Proceedings of ASME Turbo Expo 2008: Power for Land Sea and Air
GT2008
June 9-13, 2008, Berlin, Germany

GT2008-50168

EXPERIMENTAL INVESTIGATIONS AND NUMERICAL VALIDATION OF AN OUTLET GUIDE VANE WITH AN ENGINE MOUNT RECESS

Johan Hjärne
Department of Aero and Thermo Dynamics
Volvo Aero Corporation
461 81 Trollhättan, Sweden
johan.hjarne@volvo.com

Valery Chernoray
Department of Applied Mechanics
Chalmers University of Technology
412 96 Gothenburg, Sweden
valery.chernoray@chalmers.se

Jonas Larsson
Department of Aero and Thermo Dynamics
Volvo Aero Corporation
461 81 Trollhättan, Sweden
jonas.larsson@volvo.com

ABSTRACT

This paper presents experiments and CFD calculations of a Low Pressure Turbine/Outlet Guide Vane (LPT/OGV) equipped with an engine mount recess (a bump) tested in the Chalmers linear LPT/OGV cascade. The investigated characteristics include performance for the design point in terms of total pressure loss and turning as well as a detailed description of the downstream development of the secondary flow field.

The numerical simulations are performed for the same inlet conditions as in the test-facility with engine-like properties in terms of Reynolds number, boundary-layer thickness and inlet flow angle. The objective is to validate how accurately and reliably the secondary flow field and losses can be predicted for an LPT/OGV equipped with a bump.

Three different turbulent models as implemented in FLUENT, the k-ε realizable model, the kω-SST model and the RSM are validated against detailed measurements. From these results it can be concluded that the kω-SST model predicts both the secondary flow field and the losses most accurately.

1 INTRODUCTION

The aerodynamic function of low pressure turbine outlet guide vanes (LPT/OGV) is to de-swirl the flow from the low-pressure turbine into an axial flow for the design point with as low pressure loss as possible. This de-swirling generates a diffusing flow with growing boundary layers, strong secondary flows, and increases the risk of separation on the vane surfaces as well as the hub and shroud. The OGV should also perform without big pressure losses or separation in off-design conditions which makes the design procedure even more challenging. In addition to the structural requirements and weight reduction goals, recent turbine rear frame (TRF)[1] designs often require use of non-cylindrical shrouds with a three-dimensional polygonal shape and sunken engine-mount bumps. The engine mounts are often recessed into the gas channel, see Fig. 1, in order to minimize induced bending moments to the TRF case. Until recently these engine-mount bumps have only been designed structurally without any aerodynamic considerations. These bumps can protrude into the gas channel quite drastically and cover as much as 30% of the inlet span of the OGV. Without an aerodynamic design of the bumps they can cause separations with large pressure losses and residual outlet swirl, significantly reducing efficiency as a result.

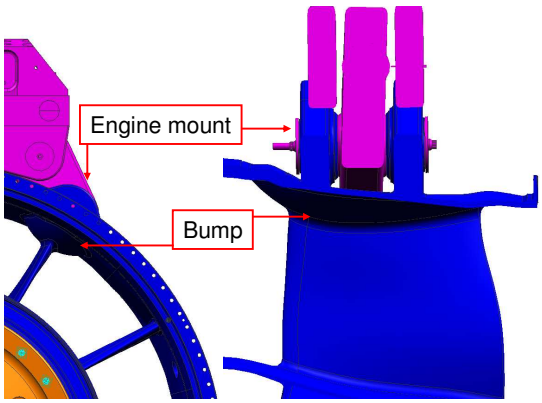

Figure 1 Turbine rear frame showing how the engine mounts are sunken into the gas channel (courtesy of Volvo Aero Corporation).

The aim of this paper is to present how three well known turbulence models in the turbomachinery field predict the flow field around an outlet guide vane with a bump. The simulations are compared to experiments performed in a linear cascade. A literature survey shows that very few, if any, measurements of realistic OGV flow-cases including bumps are publicly available.

[1] Other acronyms for this component is TBH and TEC

NOMENCLATURE

C	blade chord [m]
Cp	pressure coefficient, see Eq. [2]
P_{dyn}	dynamic pressure [Pa]
P_s	static pressure [Pa]
P_{tot}	total pressure [Pa]
Re_c	Reynolds number based on chord length
u, v, w	mean velocity components in x, y and z-direction [m/s]
x, y, z	coordinates [m], see Fig. [2]

Greek Symbols

δ_{099}	boundary-layer thickness [m]
ω_x	streamwise vorticity [1/s], see Eq. [1]
ξ	total pressure loss [%], see Eq. [3]

Subscript

fs	free stream value
mwa	mass weighted average
in	inlet conditions

Acronyms

LPT	Low Pressure Turbine
OGV	Outlet Guide Vane
TBH	Tail Bearing Housing
TEC	Turbine Exhaust Casing
TRF	Turbine Rear Frame

2 EXPERIMENTAL SETUP

The linear cascade used for these measurements is an open circuit blower type. As Fig. 2 illustrates the test section is built up of two parallel discs and two blade carriers, with the blade carriers constituting the side walls of the 7 OGV's, thus forming the cascade. The gap between the inner and outer discs is used for sucking out the boundary layers developed in the upstream sections. A 30 kW fan is used to drive the flow through a diffuser and a flow conditioner (consisting of a honeycomb and three screens with different porosity). To increase the turbulence intensity from 0.5 % to 5 % in the test-section a grid was inserted 450 mm upstream of the cascade and parallel to the leading edge, as can be seen in Fig. 2. Another issue of interest is the Mach numbers which are much lower compared to a real engine and there will be no compressible effects. However, the inlet Mach numbers for an OGV like this are quite low with a maximum Mach number at the suction side peak of around 0.6. In addition Hjärne [1] confirmed with CFD simulations that compressibility effects are small for typical OGV flows. A more detailed description of the test-facility has been given earlier by Hjärne et al. [2, 3].

2.1 DESIGN OF THE BUMP

The size of the bump is dependent on the size required for the structural considerations. The engine mounts need to be big enough and strong enough to carry the loads from the engine and position the engine mount pin close to the outer polygonal cross-section of the shroud. Hence, the size of the engine-mount bump protruding into the gas channel is fixed from the structural demands before the aerodynamic design procedure starts. The bump used in the experiment was designed as similar as possible to a real engine-mount bump. However, some geometric parameters had to be more conservative compared to a bump in an engine; the reason being that the gas channel in the engine usually is contracting. This end-wall contraction helps to accelerate the flow and thereby prevent separation from the OGV and/or the bump. Another benefit from a contracting gas channel is that a bump does not protrude into the gas channel as much as it would in a straight channel. Therefore the bump had to be designed more conservative than a real bump in order to obtain fairly realistic flow conditions in a linear cascade with straight end-walls.

To have the possibility to use exactly the same OGV in the measurements with the bump, as used in earlier investigations, [3, 4, 5, 6], the bump was designed with a hole corresponding to the vane so that the original vane profile could be passed through the bump, see Fig. 3. The geometric parameters for the bump are listed in table 1. To achieve a periodic flow field in the six passages five bumps were manufactured and placed on one of the side walls in the cascade.

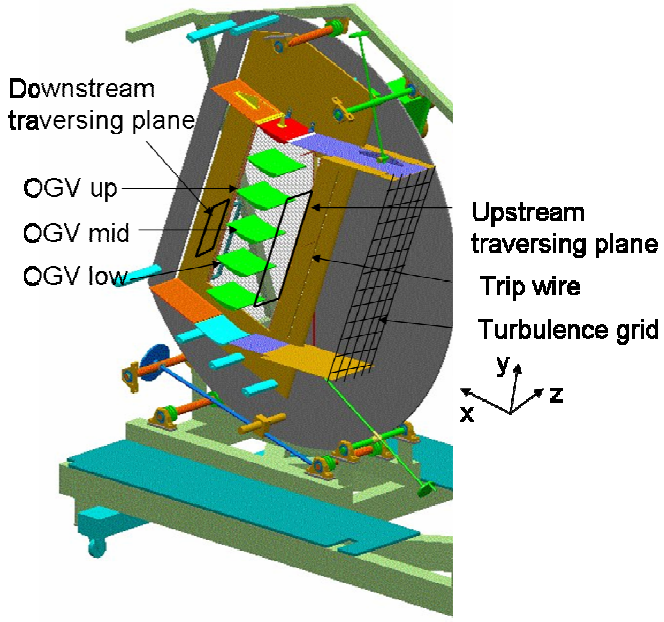

Figure 2 The experimental set up.

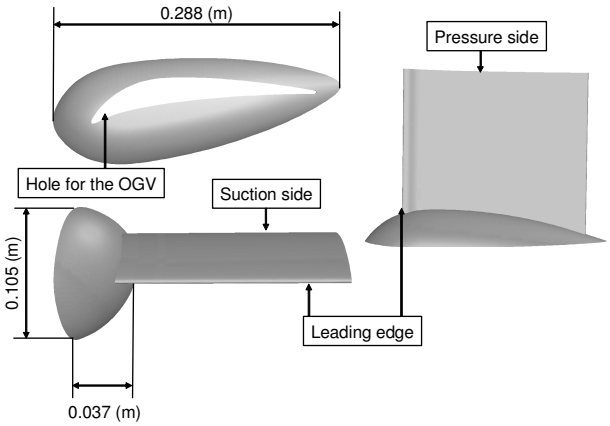

Figure 3 The experimental OGV with the bump.

Table 1 Cascade geometry data and geometrical properties for the OGV and the bump.

Number of vanes	[-]	7
Chord length	[m]	0.220
Pitch to chord ratio	[-]	0.91
Aspect ratio (Span to Chord ratio)	[-]	0.91
Inlet velocity	[m/s]	20
Inlet Reynolds number (Re_c)	[-]	280000
Inlet flow angle	[°]	30
Turbulence intensity	[%]	5
Incoming boundary-layer thickness, δ_{099}	[m]	0.0096
Bump length	[m]	0.288
Bump depth (z-direction)	[m]	0.037
Bump width (y-direction)	[m]	0.105
Bump depth / length	[%]	12.8
Bump depth / OGV span	[%]	18.5

2.2 THE TEST OBJECT

The OGV's and the bumps were manufactured with a rapid prototyping technique called SLA (Stereo lithography Apparatus) which manufactures the test objects with an accuracy of ±0.1 % of the size of the geometrical model. Because of the method by which the model is built, small traces are created on the surface when the photo-polymer hardens. These traces are filled with putty and thereafter the model is polished to obtain a hydraulically smooth surface.

The static pressure measurements on the bump were monitored with 103 static pressure taps with the majority of the holes placed on the same side as the suction side of the vane, see Fig. 4. The static pressure holes in the model had a diameter of 1mm and were connected to metal tubes on the sides of the bump and thereafter by vinyl tubes to a scanning valve system which was connected to a PSI system.

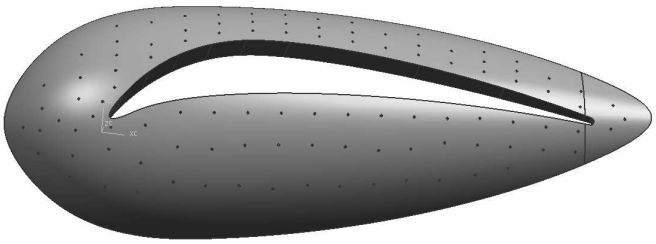

Figure 4 The bump with the static pressure holes.

Significant efforts were made to obtain a good flow periodicity in the cascade. The flow periodicity has been checked and is illustrated for the three mid vanes 8mm from the end-wall and 0.8C downstream of the trailing edge in Fig. 5.

2.3 INSTRUMENTATION AND MEASUREMENTS

Two traversing systems were used to measure the flow field both upstream and downstream. The movements in the (y, z) plane are controlled by stepper motors with an accuracy of at least 12.5 µm. The five-hole pressure probes used for the upstream and downstream traverses have been manufactured

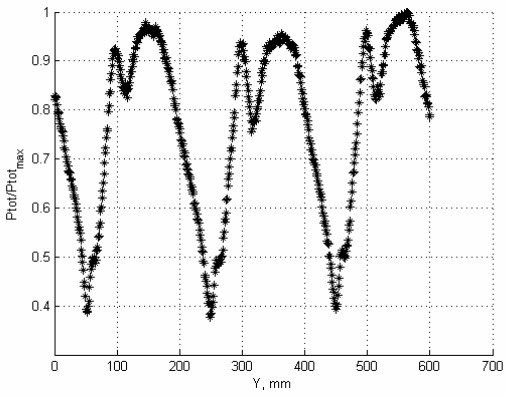

Figure 5 Normalized P_{tot} of the downstream wakes showing the periodicity at the position 8mm from the end-wall.

at Chalmers and were calibrated between –20 to 20 degrees for both pitch and yaw angles. The finite size of the probe head diameter was 3.5 mm with an individual distance between the holes of 1 mm.

The inlet measurements were conducted at an axial position of -0.3C upstream the cascade inlet plane with a resolution of the flow field of 20 mm (10 % pitch) in y and z direction. The upstream traversing system, equipped with a hot wire, was also used to measure the incoming boundary layer height along the side walls. The boundary layer was measured in the flow direction 0.91C upstream of the leading edge plane, it was fully turbulent and had a thickness of 9.6 mm (δ_{099}).

As the cascade produce a flowfield which has a very good periodicity and symmetry, earlier described by Hjärne et al. [3], the outlet measurements were taken over half of the span one pitch length over the central vane and bump (140 mm below the trailing edge to 60 mm above the trailing edge) at three different streamwise locations downstream of the trailing edge (0.25C, 0.5C and 0.8C). An experimental grid of 2 mm in each direction was used. To avoid wall proximity effects, as suggested in [7], the flow field was not measured at a distance lower than two times the five-hole probe head size from the endwall. All tests were performed with the same inlet flow angle, α=30 °, which is the design point for the investigated OGV.

3 NUMERICAL CALCULATIONS

The 3D CFD calculations were preformed with the numerical software tool FLUENT (v. 6.2.16) [8]. Three different turbulence models, k-ε realizable model, k-ω SST model, and the RSM have been used and compared with experimental results. In earlier investigations by Hjärne et al [4] the Spalart-Allmaras model was investigated as well. However, in this investigation the Spalart-Allmaras model produced unsatisfactory results for these kinds of flows and therefore this model was neglected in this study.

The mesh generator used was ICEM-HEXA and a side view of the computational domain for the calculations is depicted in Fig. 6. The inlet boundary condition was placed 0.9C upstream of the blade leading edge and the outlet boundary condition was placed 0.9C downstream of the trailing edge.

A mesh dependence study was performed using two different mesh sizes. The baseline mesh had $2.4*10^6$ mesh cells and the refined mesh had $3.3*10^6$ cells. The turbulence

model used for this study was the k-ε realizable model with resolved boundary layers.

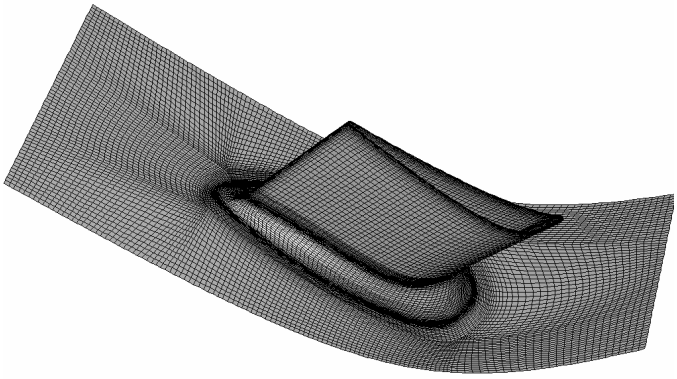

Figure 6 The 3D mesh for the bump domain consisting of $2.4*10^6$ cells.

To check the grid sensitivity the mass averaged total pressure losses over the OGV, ξ_{mwa}, were calculated at 3 downstream positions between 0.25C and 0.8C of the OGV trailing edge. The difference in pressure loss between the mesh sizes was marginal and therefore the baseline mesh was considered to be sufficiently refined in order to obtain results which were independent of the grid.

Turbulence Modeling

The flow field around OGVs with bumps is diffusive and together with growing boundary layers both on the end walls and also on the vane and bump the risk of separation is high. In terms of turbulence modeling this is a challenging case to predict. Below there is a short description of the three turbulence models used and also for the enhanced wall treatment used for the k-ε realizable model and the RSM:

Shih's realizable k-ε model [9]

This is the most commonly used turbulence model in FLUENT. It is similar to the classical k-ε model but has a variable C_μ and a modified ε equation. The main advantage with the Realizable version for the present application is that it has better performance, in terms of predicting the production of k, compared to a classical k-ε model in regions with strong deceleration and acceleration, for example in the leading edge region and the region around the suction side pressure minimum. Note that this is a high-Re model which needs to be complemented with a low-Re model close to the walls if a grid with resolved boundary layers is used.

Menter's kω-SST model [10, 11]

This model has become increasingly popular in the last few years and it is now regarded a standard model in the turbomachinery field. It is a low-Re model which performs well with resolved boundary layers. The kω-SST model has been known to work especially well for cases with adverse pressure gradients and separations. It is also commonly used in heat-transfer applications.

RSM [12, 13, 14]

The Reynolds Stress Model solves the Reynolds stresses using individual transport equations. This model account for the effects of streamline curvature and rapid changes in the strain rate in a more rigorous manner than the two equation models and therefore it has a good potential to give accurate predictions for these kinds of flows.

Enhanced wall-treatment/two-layer model [15, 16, 17]

When used on fine grids with resolved boundary layers (y+ < 1) this model employs a Wolfstein [15] one-equation model in the inner parts of the boundary layers. This model is matched to the k-ε model in the outer region following the work by Jongen [16]. The length-scale is computed according to Chen & Patel [17]. This two-layer approach is very attractive. It avoids the ad-hoc damping functions used in many other low-Re models and it seldom leads to any numerical problems. For cases with large separations and 3-dimensional boundary layers, the low-Re two-layer model is normally superior to a wall-function approach.

The FLUENT simulations were computed for incompressible, viscous, low-speed conditions with inlet velocity profiles taken from the measurements. All calculations where conducted with resolved boundary layers and were run with a segregated double precision solver and a second order upwind scheme.

4 RESULTS AND DISCUSSION

Complete investigations of an OGV downstream passage have been made with a 5-hole pressure probe. A time mean value of the flow field variables can thus be deduced. Besides the losses and outlet flow angles, by employing a high plane discretization, it was possible to compute the streamwise vorticity according to Eq. 1.

$$\omega_x = \frac{\partial w}{\partial y} - \frac{\partial v}{\partial z} \tag{1}$$

4.1 LOAD DISTRIBUTION FOR THE BUMPS

In Fig. 7 the Cp distribution, calculated as Eq. 2, for the bump is shown for the experiments and the calculations. The comparison shows that the results are very similar.

$$Cp = \frac{P_{tot,in} - P_s}{P_{dyn,in}} \tag{2}$$

- The stagnation point at the front part of the bump is located at the same place for both the calculations and the experiment. The minimum value in the experiment is slightly higher compared to the calculations. This is not surprising since it would be necessary to have a pressure tap exactly in the stagnation point to capture the same value in the stagnation region as the calculation. This is difficult to achieve.
- Continuing with the suction side peak its location and extension is also very similar. Again the extreme value is somewhat lower in the experiment compared to the CFD. This is again due to that the pressure taps are not positioned at the precise minimum pressure point in the suction side corner.
- After the suction peak the Cp distribution is almost identical between the experiment and the calculations.
- The pressure side part of the bump is also very well predicted.

It seems that the numerical models are able to predict the pressure distribution very well. Even though the flow around the rear bump-part on the suction side of the OGV is highly three-dimensional and complex the models predict the pressure distribution satisfactorily.

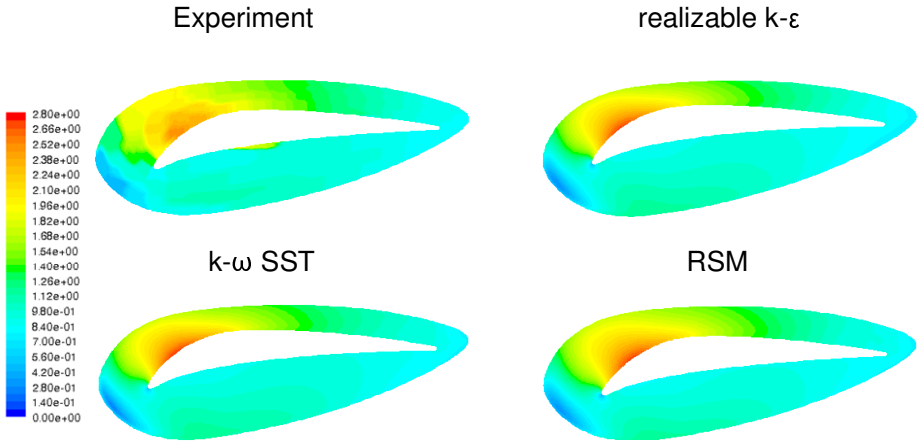

Figure 7 Comparison in Cp distribution for the bump.

4.2 DOWNSTREAM WAKE PROFILES

Figure 8 compares the wake distribution obtained from the experiment compared to the CFD calculations at four different spanwise positions at 0.8C downstream of the trailing edge. To increase the understanding of the downstream wake plots Fig. 9 shows contour plots of the normalized downstream total pressure with white lines indicating the spanwise positions. In Fig. 9, line (a) represents the wake measurement 8mm from the end-wall, line (b) 24mm from the end-wall, line (c) 50mm from the end-wall and finally line (d) is at mid-span.

As Fig. 8 shows, the wake at mid-span is accurately predicted by all the numerical models. The realizable k-ε model predicts the depth of the wake very well but misses slightly on the width, where it overpredicts the size of the suction side boundary-layer growth. The RSM captures the width of the wake very well but misses slightly on the depth and the k-ω SST model predicts both the depth and the width very accurately. When comparing the wake plots in Fig. 8 with the contour plot in Fig. 9 the same tendencies are seen. The realizable k-ε model and the k-ω SST model show a slightly higher pressure in the wake compared to the RSM at mid-span.

For the wake distribution 50mm from the bump-end-wall in Fig. 8 some interesting observations can be made. At this position the wake is wider compared to the mid-span case but it has a similar depth which also is visible in the contour plot in Fig. 9. As can be seen in this figure there is an unloading in the wake between line (b) and (c) for the experiment. This unloading is due to the secondary flow field developed in the corner region of the suction side and the bump (further explained in paragraph 4.4). The measurement line (c) is just behind the thickest part of the OGV-wake where the wake is wider compared to the mid-span position.

Considering the turbulence models they all over predict the depth of the wake as shown in Fig. 8. The reason for this behavior is that the models do not compute the evolution of the secondary flow field correctly and therefore the unloading in the wake between line (b) and (c) in Fig. 9 is incorrectly predicted. Hence, at the position where the wake is evaluated the numerical models show a deeper wake which is clear in Fig. 8. The best prediction again comes from the k-ω SST model which gives a slightly less deep and wide wake compared to the other models. This is even better understood from Fig. 9 where it can be seen that the kω-SST model is closest to the experimental results.

At 24mm from the sidewall the experiment in Fig. 8 shows both the wake from the OGV and also the wake created by the suction side part of the bump called "*ss-bump-wake*". It is also evident that while these two wakes have joined, the part from the OGV is less deep compared to the other two spanwise positions and it is now the ss-bump-wake which is the dominant wake. Again this is well depicted in the contour plots in Fig. 9. In the experiment two wakes are visible, firstly the ss bump-wake at $y \approx 0.27$m and secondly the wake from the OGV at $y \approx 0.29$m.

As for the earlier two span positions the numerical models predict the start of the OGV-wake on the pressure side very well but none of the models show the influence from the ss-bump-wake explicitly in Fig. 8. Looking in Fig. 9 it can be seen that the k-ω SST model and the RSM show the bulb shaped ss-bump-wake close to the end-wall at $y \approx 0.27$m but it does not extend as far spanwise as the experiment and therefore this wake is not visible in Fig. 8. Considering the k-ε realizable model it shows a more solid wake all the way from the end-wall towards midspan with a vague unloading between line b and c.

For the position closest to the end-wall in Fig. 8 the experiment shows that the wake from the OGV and the ss-bump-wake are now almost fully joined. With measurements made so close to the wall, the bump-wake arising from the pressure side of the vane, called "*ps-bump-wake",* is also visible. This wake is the smallest one and positioned at $y \approx 100$mm to 140mm. Even though it is not clear a small spot of lower total pressure can be viewed for the experiment in Fig. 9 at $y \approx 0.32$m which represents the pressure side part of the bump wake.

When comparing the numerical results in Fig 8 with the experiments, it is the k-ω SST model that shows the best results. Starting from the top position at y=200mm this model follows the experimental results to the position where the ps-bump-wake occurs, however, the model does not capture the ps-bump-wake. A small lowering of the pressure can be seen around $y \approx 110$mm but it is obvious that the span wise extension of the ps bump-wake for the kω-SST model is weaker compared to the experiment. After the ps-bump wake the result from the kω-SST model follows the experimental curve satisfactorily.

The RSM does not follow the experimental results as well as the kω-SST model from the top position. The values are significantly lower compared to the experiment and the RSM totally miss the ps bump-wake. Thereafter the RSM captures the start of the big joined wake from the OGV and ss-bump-wake at $y \approx 95$mm but it misses the suction peak of the ss-bump-wake.

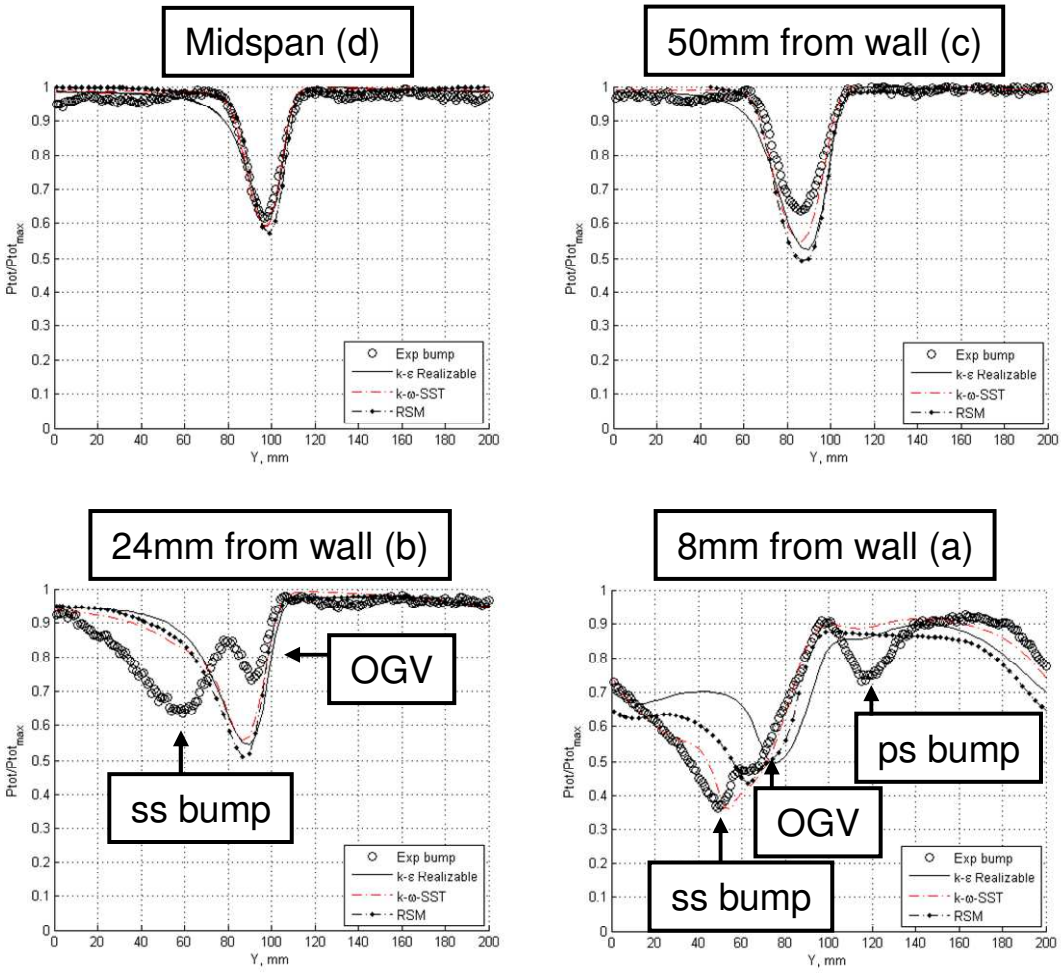

Figure 8 Wake distributions from mid-span to 8mm from the end-wall 0.8C downstream of the trailing edge

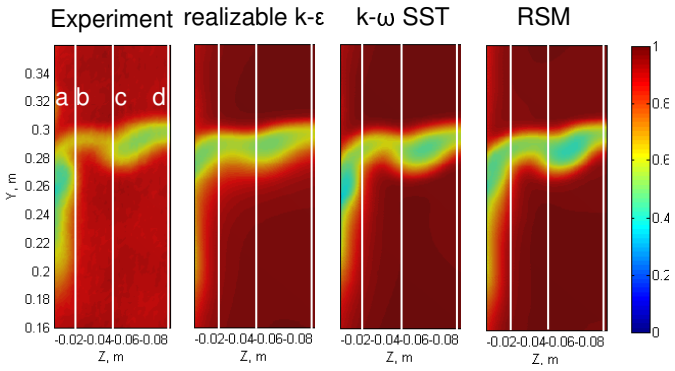

Figure 9 Normalized total pressures where the white lines show the measuring position for the wake plots in Fig. 8.

Considering the realizable k-ε model there are even greater deviations. Starting from the top it is somewhat closer to the experiment compared to the RSM and this model shows a lowering of the value in the region where the ps bump-wake is positioned, but this lowering continues and also the start of the big joined wake at y ≈ 95mm is miss predicted. This model also shows greater deviations compared to the other models for the rest of the wake. Not so much more information is gained from Fig. 9 in this case.

It should be mentioned here that the flowfield in the corner of the suction side and the bump is very complex. Simple visualizations with wool tufts in the experiment show that strong secondary flows arise in the corner of the suction side and the bump. All the numerical models predict some degree of separation in this region both on the bump and on the OGV. Because of this separation the models have problems in predicting the correct development of the secondary flowfield.

4.3 OUTLET PITCH ANGLES

Residual swirling flow exiting the LPT/OGV will further downstream create more total pressure losses. Therefore it is important to investigate the outlet pitch angle. The mass averaged spanwise pitch angle distribution 0.8C downstream of the trailing edge is presented in Fig. 10.

Close to the end-wall the flow in the experiment is under-turned with approximately 1 degree. Moving towards mid-span the outlet flow angle in the experiment continues to decrease and reaches its minimum angle at span = -0.05m before it starts to increase and at mid-span it reaches 1 degree of under-turning. A usual design goal for LPT/OGVs, without a bump, is to have an outlet pitch angle around 0 degrees which implies that the bumps make it harder for the OGV to reach this design goal.

The numerical results manage to predict the pitch angle distribution rather accurately. The realizable k-ε model and the RSM never differ more than 0.5 degrees from the experiment. The k-ω SST model also predicts the angles very well. Even though the integrated values differ more from the experiment compared to the other models the k-ω SST model captures the trends in the angle distribution

better. Close to the end-wall an overshoot is visible, also visible in the experiment at span = -0.01m, and after that the curve from the kω-SST model follows the exact same shape as the measured values towards mid-span but at an angle which is 1 degree lower at its most.

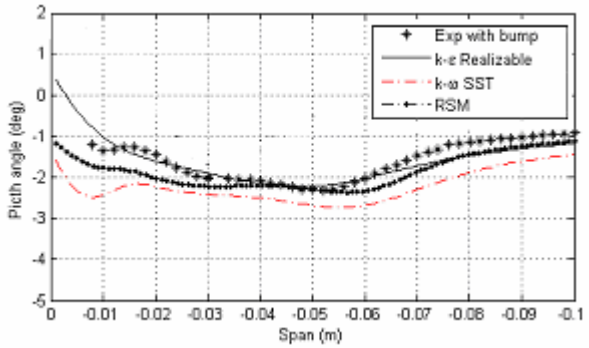

Figure 10 Mass averaged spanwise pitch angles at downstream position x=0.8C.

4.4 DOWNSTREAM DEVELOPMENT OF THE SECONDARY FLOWFIELD

For better explanations of the development of the secondary flow field two sketches, Fig. 11 and Fig. 12, describe the evolution of the streamwise vorticity in the flow passage. The blue color in these figures describes areas of negative vorticity and the red color shows the positive vorticity regions. The numbering for Fig. 11 and 12 is also used in Fig. 13 which depicts the experimental results of the calculated streamwise vorticity at the three downstream positions behind the trailing edge. The numbering for the three figures is explained below:

1. **Pressure side leg of the horse shoe vortex.** This vortex is created from the incoming boundary-layer which wraps itself around the leading edge at the bump and is transported downstream as is visualized in Fig. 12.
2. **The pressure gradient**, depicted at the end-wall in Fig. 12, arises due to the pressure difference between the pressure side and the suction side of the OGV. The pressure gradient transports the flow from the pressure side towards the suction side along the end-wall. The low momentum fluid closest to the wall is more affected by the pressure gradient and a two parted boundary layer is developed with both an accelerating part and a decelerating part which is shown in Fig. 11. In the accelerating part of the boundary layer a positive, anti clock wise rotating, vorticity region is developed which is shown as the area closest to the end-wall. This red vorticity region is not visible in the experimental results in Fig. 13 since it is outside of the measuring region as shown in Fig. 11.
3. **Negative boundary-layer vorticity.** This is the blue region outside the red region close to the end-wall, and is developed from the decelerating part of the above mentioned end-wall boundary layer.
4. **Accumulated negative boundary-layer vorticity.** This is an accumulation from the negative boundary-layer vorticity from the end-wall boundary layer and also from the same type of boundary-layer vorticity developed on the bump and on the suction side of the OGV. The development is shown in Fig. 11.
5. **Blade shed vorticity/blade shed vortex.** When the end-wall flow developed from the pressure gradient meets the bump and the suction side of the OGV it gets deflected towards mid-span. Hence a new boundary layer starts to grow at the bump and the OGV and a similar type of boundary layer as at the end-wall is developed. Again a positive vorticity region is developed closest to the bump and the OGV which is depicted in Fig. 11 and Fig. 14.
6. When the flow field along the vane meets the same flow field developed on the opposite end-wall at mid-span it is deflected downwards and a large scale circular motion is developed as shown in Fig. 11.

Figure 13 shows the calculated vorticity of the experimental results from the downstream measurements. These downstream measurements clearly show all the major vortical structures from the schematic pictures Fig. 11 and Fig. 12 and also how they develop from the trailing edge and downstream.

Starting with the position closest to the trailing edge it is obvious how the negative part of the boundary-layer vorticity, No 3, starts to grow at pitch position $y \approx 0.16$m and around pitch position $y \approx 0.19$m a more intense region is shown which is the pressure side leg of the horse shoe vortex, No. 1. The negative part of the boundary-layer vorticity continues to grow up to $y \approx 0.25$m and from this position the feeding of the negative boundary-layer vorticity to the accumulated vorticity region, No 4, is visible and highlighted in the figure. The accumulated negative boundary-layer vorticity is deflected towards midspan by the bump. The reason for this behavior is that when the flow field close to the end-wall, driven by the pressure gradient No 2 in Fig. 12, meets the bump it simply follows the bump towards mid-span and therefore pushes the negative accumulation of the boundary-layer vorticity towards midspan. Finally the blade shed vorticity from the OGV and the bump is the red region at $y \approx 0.29$m. Close to the end-wall the blade shed vorticity is deflected downwards due to that the OGV is not capable of deflecting the flow in the vicinity of the bump. Figure 14 shows that when the OGV does not manage to deflect the flow the blade shed vorticity, No 5, is penetrating the boundary-layer vorticity, No 3, and the accumulated negative boundary-layer vorticity, No 4 and pushes the latter towards midspan.

Going further downstream to x = 0.5C the blade shed vorticity starts to divide into two separate vorticity regions, No. 5a and 5b. The most intense region remains close to the sidewalls and is drawn downwards, as explained above. The other part of the blade shed vorticity and the accumulated negative boundary-layer vorticity, No 4, are moving towards mid-span and at the same time they are dissipating.

At the position furthest downstream no major differences are seen. The blade shed vorticity is now divided into two separate vorticity regions and No 5a close to the end-wall has now grown even bigger and is keeping its intensity intact. This vorticity region is sucking in low momentum fluid from the wake which makes it thinner and this is why the unloading in the wake occurs. The weaker parts of the blade shed vorticity and the accumulated negative boundary-layer vorticity continue to dissipate and moves further spanwise.

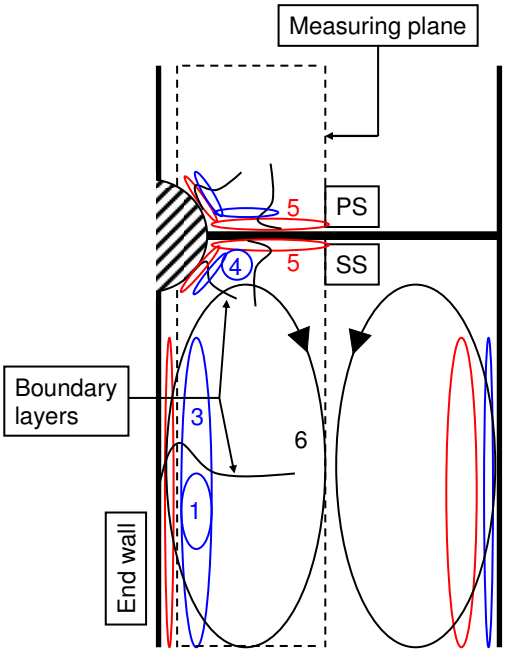

Figure 11 Schematic picture of the development of the different vortical structures in the flow passage.

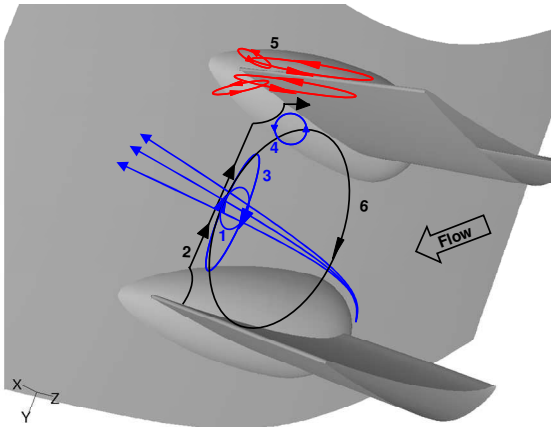

Figure 12 Explanation of the development of the vortical structures in the flow passage.

Figure 15 compares the streamwise vorticity for the experiment and the three numerical models at the downstream position x = 0.8C. As can be seen in the figure there are some differences between the models and the experiment.

- The realizable k-ε model seems to be the most diffusive model and shows the lowest magnitudes and least extension of the streamwise vorticity compared to the experiment and the other numerical models. Compared to the experiment all the major vortical structures are weaker and some of them are barely visible.
- The k-ω SST model resolves the secondary flowfield better compared to both the realizable k-ε model and the RSM. The pressure side leg of the horse shoe vortex has a similar magnitude compared to the experiment and the model also predicts this vorticity region at approximately the same pitchwise location (y-position) which the other models miss. The blade shed vorticity is well predicted and the division into two separate vorticity regions, 5a and 5b, is better pronounced compared to the other two models. The accumulated negative boundary-layer vorticity is also close to the experimental results both in terms of position and magnitude.
- The RSM predicts some parts of the streamwise vorticity very accurately compared to the experiments. The part of the blade shed vorticity close to the end-wall, No 5a, is very close to the experiment both regarding position and size. The other part of the blade shed vorticity close to mid-span, No 5b, is also comparable to the experiment as well as the accumulated negative boundary-layer vorticity. Even though these vortical structures are well predicted the RSM misses to predict the pressure side leg of the horse shoe vortex which does not have the same intensity as the experiment or the k-ω SST model.

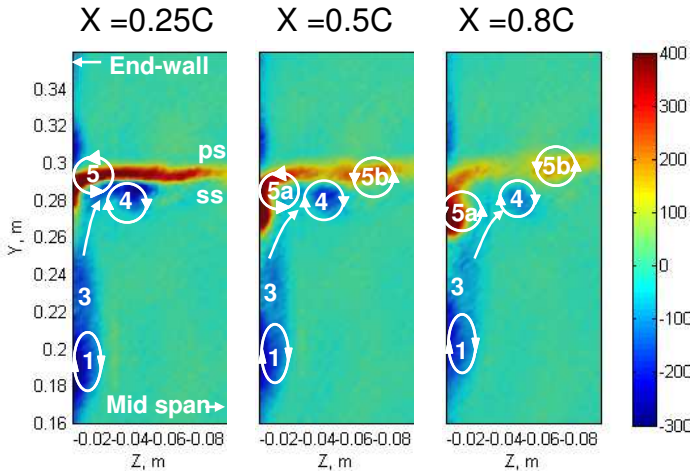

Figure 13 Streamwise vorticity for the three downstream positions.

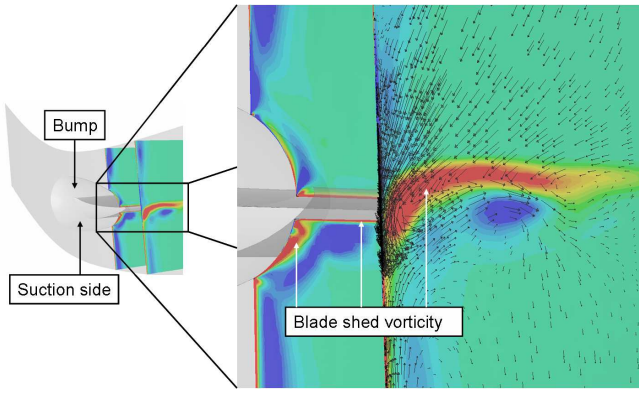

Figure 14 CFD calculations with the RSM showing how the blade shed vorticity is drawn downwards.

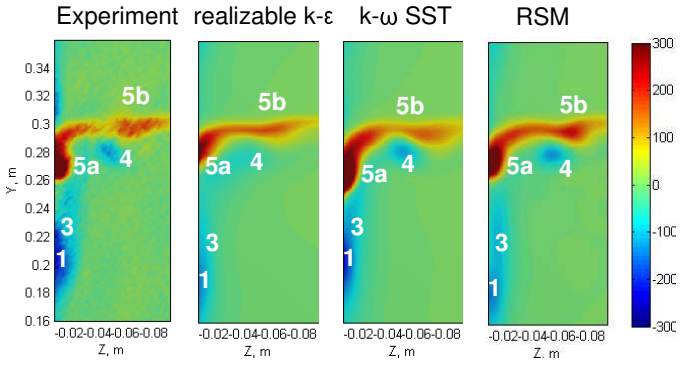

Figure 15 Streamwise vorticity for the experiment and the CFD calculations.

4.5 PITCHWISE MASS AVERAGED LOSSES

The experimental and numerical results for the mass averaged pitchwise losses at position 0.8C downstream of the trailing edge are presented in Fig. 16. The losses are calculated according to Eq. 3

$$\xi_{mwa} = \frac{P_{tot} - P_{tot,fs}}{P_{dyn,in}} \qquad (3)$$

To understand how the losses are related to the secondary flow field the vortical structures have been inserted into the Fig. 16 to explain the shape of the loss curve.

From the end-wall to span position = -0.035m there is a decay in the losses which is natural since the losses are at their highest close to the end-wall where the boundary layers are developed. Between span -0.025m and -0.04m is where the wake is thinnest due to the secondary flows field around the bump, also shown in the contour plot in Fig. 9. After span position -0.04m the losses start to increase again and reach a maximum value at span position -0.065m. This is where the accumulated boundary-layer vorticity, No 4, and the other part of the blade shed vorticity, No 5b, are positioned. At this position the wake developed by the OGV has its thickest part, also visible in Fig. 9. After this the wake thins out towards mid-span and the values for the losses diminish.

When comparing the experimental results with the CFD calculations some differences can be noticed:

- the realizable k-ε model shows similar results compared to the experiment in the end-wall region. At span position -0.02m the loss curve deflects towards mid-span and reaches a maximum at span position -0.055m. From this position it decays towards mid-span and ends at a loss of about 4% at mid-span. The loss curve from the k-ε realizable model does not follow the experimental curve as well as the other two models which is due to its dissipative nature.
- The k-ω SST model predicts the pitchwise averaged losses very well. It follows the experimental curve from the end-wall towards its minimum value but rises earlier compared to the experiment. At its highest value, span -0.065m, it has slightly higher losses compared the experiment and thereafter it follows the two other numerical curves towards mid-span. The k-ω SST model predict a loss curve which is very close to the experiment and better compared to the other two models, which is due to its superior prediction of the secondary flowfield.
- The RSM predict the decay of the loss close to the end-wall very well, but it does not follow the experimental curve towards its minimum value. Instead the RSM predict an increase of loss again towards mid-span and peak at the same span position, -0.065 mm, as the experiment but at a higher value. Thereafter the loss decreases again towards mid-span to the same value as the other models.

Figure 17 shows the mass averaged losses for all three downstream positions. For the numerical models the k-ω SST model is closest to the experimental results and the RSM overpredicts the losses the most. From a design point of view it is good that the losses are overpredicted instead of underpredicted since this leads to a conservative design.

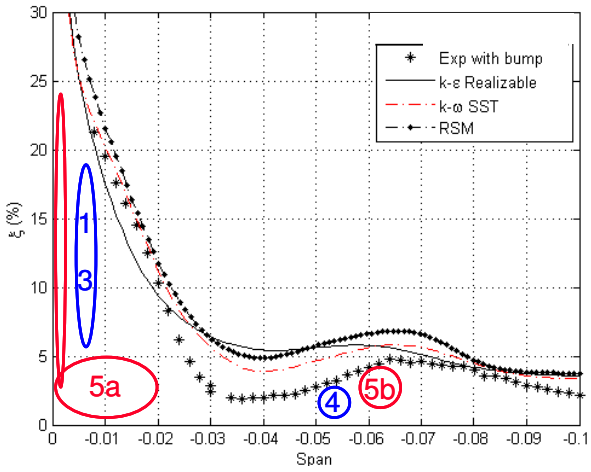

Figure 16 Pitchwise average of the losses at X=0.8C.

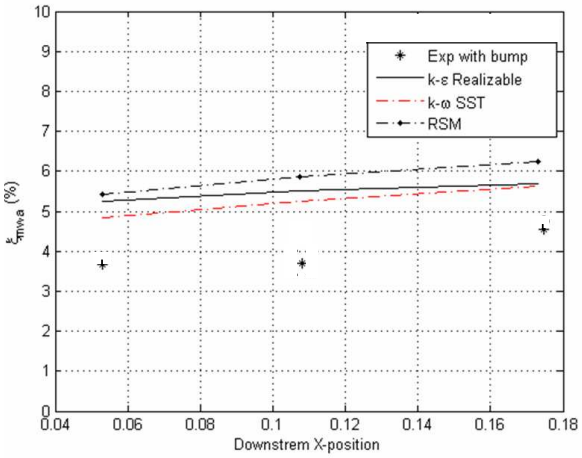

Figure 17 Mass averaged outlet losses for the three downstream planes.

5 CONCLUSIONS

In this paper experiments and numerical simulations of the flow field around an engine mount bump was analyzed. Bump flows are essential when designing OGVs and therefore these results are of great interest. For the measurements in the cascade, three numerical models as implemented in Fluent, are validated to find a model that is most appropriate to use for new designs of bump flows. Below is a summary of their strengths and weaknesses for OGV-bump flows.

<u>The realizable k-ε model</u>

The realizable k-ε model is a commonly used model in the turbomachinery field and it is known to perform well regarding the production of turbulent kinetic energy in regions with strong deceleration and acceleration. In this paper this model has produced decent results. The model does not resolve secondary flow field as well or as thoroughly as the other two models because of its dissipative nature. Another drawback is that it overpredicts the boundary-layer growth on the suction side of the OGV. Finally this model has shown to be the most robust model, meaning that there were never any problems with convergence and in CPU-hours this was the most economical model.

The k-ω SST model

The k-ω SST model has increased in popularity in the turbomachinery field and from the results of the validation in this paper this is understandable. This model has shown very good results in terms of Cp predictions, downstream wake distributions and especially in predicting the secondary flow development. The model was also fairly robust and fast in terms of CPU hours.

RSM

This model has a good potential in predicting OGV bump flows. It takes into account the effect of streamline curvature and rapid changes in the strain rate in a more rigorous manner compared to the other two models. By any standard, the RSM showed good results. But one big drawback for the RSM is the robustness. It took some time to get it to converge properly and when it did converge the number of CPU hours needed was much higher compared to the other two models.

As a final remark the author would recommend the use of the kω-SST model for thorough investigations of the flowfield for bump flows. This model is superior to the other models when it comes to predicting the progress of a secondary flowfield and was many times used by the authors to increase the understanding of the experimental results.

REFERENCES

[1] Hjärne, J., 2001, "Aerodynamic Analysis of Outlet Guide Vane Flows," Diploma thesis, Chalmers University of Technology, Göteborg, pp. 35-36

[2] Hjärne, J., Larsson, J. and Löfdahl, L., 2003, "Design of a Modern Test-Facility for LPT/OGV flows," ASME paper GT2003-38083

[3] Hjärne, J., Chernoray, V., Larsson, J. and Löfdahl, L., 2005, "Experimental Evaluation of the Flow Field in a State of the Art Linear Cascade with Boundary-Layer Suction," ASME paper GT2005-68399

[4] Hjärne, J., Larsson, J. and Löfdahl, L., 2006, "Performance and Off-Design Characteristics for Low Pressure Turbine Outlet Guide Vanes: Measurements and Calculations," ASME paper GT2006-90550

[5] Hjärne, J., Chernoray, V., Larsson, J. and Löfdahl, L., 2006, "An Experimental Investigation of Secondary Flows and Loss Development Downstream of a Highly Loaded Low Pressure Turbine Outlet Guide Vane Cascade," ASME paper GT2006-90561

[6] Hjärne, J., Chernoray, V., Larsson, J. and Löfdahl, L., 2007, "Numerical Validations of Secondary Flows and Loss Development Downstream of a Highly Loaded Low Pressure Turbine Outlet Guide Vane Cascade," ASME paper GT2007-27712

[7] Arts, T., Boerrigter, H., Buchlin, J.-M., Carbonaro, M., Degrez, G., Dénos, R., Fletcher, D., Olivari, D., Riethmuller, M.L., Van den Braembussche, R.A., "Measurement Techniques in Fluid Mechanics", 2nd revised edition, reprint of VKI LS 1994-01.

[8] FLUENT 6, 2001, Users manual, Fluent Incorporated, Lebanon, NH, USA

[9] Shih, T.-H., Liou, W. W., Shabbir, A. Z., Yang, and Zhu, J., 1995, "A New Eddy-Viscosity Model for High Reynolds Number Turbulent Flows - Model Development and Validation", *Computers Fluids*, 24(3), pp 227-238

[10] Menter, F. R., 1994, "Two-Equation Eddy-Viscosity Turbulence Models for Engineering Applications", *AIAA Journal*, 32(8), pp 1598-1605

[11] Menter, F. R., Kuntz, M. and Langtry, R., 2003, "Ten Years of Experience with the SST Turbulence Model", in Hanjalic, K., Nagano, Y. and Tummers, M., editors, *Turbulence, Heat and Mass Transfer 4*, pp 625-632, Begell House Inc.

[12] Gibson, M. M. and Launder, B. E., 1978, "Ground Effects on Pressure Fluctuations in the Atmospheric Boundary Layer", 1978, *J. Fluid Mechanics*, 86 pp 491-511.

[13] Launder, B. E., "Second-Moment Closure: Present and Future?", 1989, *Int. J. Heat Fluid Flow*, 10(4) pp 282-300.

[14] Launder, B. E., Reece, G. J. and Rodi, W., 1975, "Progress in the Development of a Reynolds-Stress Turbulence Closure", 1975, *J. Fluid Mechanics*, 68(3) pp 537-566.

[15] Wolfstein, M., 1969, "The Velocity and Temperature Distribution of One-Dimensional Flow with Turbulence Augmentation and Pressure Gradient", *Int. J. Heat Mass Transfer*, 12 pp 301-318.

[16] Jongen, T., "Simulation and Modeling of Turbulent Incompressible Flows", 1992, PhD thesis, EPF Lausanne, Lausanne, Switzerland.

[17] Chen, H. C. and Patel, V. C., 1988, "Near-Wall Turbulence Models for Complex Flows Including Separation", *AIAA Journal*, 26(6):641-648.